Available online at www.sciencedirect.com
ScienceDirect
Nuclear Physics B Proceedings Supplement 00 (2014) 1–7
Nuclear Physics B Proceedings Supplement

CMS Detector Performance during LHC Run 1 and projections for Run 2

Silvia Goy López for the CMS Collaboration

CIEMAT, Madrid, Spain

Abstract

The performance of CMS detector during LHC Run 1 is presented. Excellent results regarding the CMS detector triggering capabilities and its performance for tracking and vertexing, particle identification, reconstruction and energy measurement, as well as jet and $\vec{E}_{\mathrm{T}}$ reconstruction have been obtained. Planned detector improvements for next LHC running period are also discussed.

Keywords:
LHC, CMS, Detector, tracker, calorimetry, Muon System, trigger

1. Introduction

The Compact Muon Solenoid (CMS) is one of two general purpose detectors at the LHC. The central feature of the CMS apparatus is a superconducting solenoid of 6 m internal diameter, providing an axial magnetic field of 3.8 T. Within the solenoid volume are a silicon pixel and strip tracker, a lead tungstate crystal electromagnetic calorimeter (ECAL), and a brass and scintillator hadron calorimeter (HCAL), each composed of a barrel and two endcap sections. Muons are measured in gas-ionization detectors embedded in the steel flux-return yoke outside the solenoid. Extensive forward calorimetry complements the coverage provided by the barrel and endcap detectors. The CMS experiment has been designed with a two-level trigger system, the Level-1 Trigger (L1), implemented through custom-designed electronics, and the High Level Trigger (HLT), a streamlined version of the CMS offline reconstruction software running on a computer farm. A more detailed description of the CMS detector, together with a definition of the coordinate system used and the relevant kinematic variables, can be found in Ref [1].

During LHC Run 1 (2010-2012 running period), pp collisions were produced at centre-of-mass energies up to 8 TeV with 50 ns bunch spacing. This resulted in nearly 30 fb^{-1} of integrated luminosity delivered to CMS, about 90% of which has been used for publications. Peak luminosities reached more than 7×10^{33} cm^{-2} s^{-1}, with an average of 21 events per bunch crossing (pileup) in 8 TeV data. Out of the 80 million channels in the CMS detector, a fraction close to 98% was active at the end of Run 1.

The LHC will re-start operations during spring of 2015, with pp collisions occurring at centre-of-mass energies of 13 TeV and bunch spacing of 25 ns. Peak luminosities of 1.4×10^{34} cm^{-2} s^{-1} could be achieved already during the first year, eventually reaching 2×10^{34} cm^{-2} s^{-1} , twice the instantaneous luminosity CMS was originally designed for. In order to cope with this harsher environment changes have been planned in the CMS detectors, to be carried out during the long shutdown period (LS1, 2013-2014) and through the Run 2 period (2015-2018).

In this paper highlights of the CMS detector performance during LHC Run 1 are presented, together with details on the main planned improvements envisaged for Run 2.

2. Tracker: Silicon Pixel and Strips

The CMS Tracker consists of two main detectors: a silicon pixel detector, covering the region from 4 to

15 cm in radius, and 49 cm on either side of the collision point along the LHC beam axis, and a silicon strip detector, covering the region from 25 to 110 cm in radius, and within 280 cm on either side of the collision point along the LHC beam axis.

The CMS silicon pixel detector has 66 million active elements instrumenting a surface area of about 1 m^2. It provides the determination of three high precision three-dimensional points on track trajectories. The detector consists of three concentric cylindrical barrel layers and four fan-blade disks closing the barrel, two on each end.

The CMS silicon strip detector has 9.3 million active elements instrumenting a surface area of 198 m^2, and consists of three large subsystems. The Tracker Inner Barrel and Disks (TIB/TID) deliver up to four r-ϕ measurements on a trajectory using 320 μm thick silicon microstrip sensors, which have their strips oriented parallel to the beam axis in the barrel and oriented radially in the disks. The TIB/TID is enclosed within the Tracker Outer Barrel (TOB) which consists of six barrel layers of 500 μm thick microstrip sensors with strip pitches of 183 μm in the first four layers and 122 μm in the last pair of layers. The Tracker EndCaps (TEC) instrument the region $124 < |z| < 280$ cm and $22.0 < r < 113.5$ cm. Each TEC is composed of nine disks that are instrumented with up to seven rings of radial-strip silicon detectors. The inner two layers of the TIB and TOB, the inner two rings of the TID and TEC, and the fifth ring of the TEC include a second microstrip detector module that is mounted back-to-back at a stereo angle of 100 mrad to provide a measurement of the orthogonal coordinate. Assuming fully efficient planes and not counting hits in stereo modules, there are from 8 to 14 high precision measurements of track impact points for $|\eta| < 2.4$.

The performance of the tracker detector has been measured in detail using 2011 data and simulation [2]. The hit efficiency is defined as the probability to find a cluster in a given silicon sensor that has been traversed by a charged particle. In the pixel detector, the efficiency is measured using isolated tracks originating from the primary vertex. The p_T is required to be > 1 GeV, and the tracks are required to be reconstructed with a minimum of 11 hits measured in the strip detector. The average efficiency for reconstructing hits in the pixel detector is $> 99\%$, when excluding from the measurement the 2.4% of modules known to be defective. The hit efficiency depends on the instantaneous luminosity and on the trigger rate, as shown in Fig. 1. Several sources of loss have been identified. First, the limited size of the internal buffer of the readout chips causes a dynamic inefficiency that increases with the instantaneous luminosity and with the trigger rate. Single-event upsets temporarily cause loss of information of approximately two readout chips per hour at a negligible rate. Finally, readout errors signalled by the off-detector modules depend on the rate of beam induced background. Some of these losses will be addressed with the replacement of the pixel detector at the end of 2016. The new pixel detector will seek to reduce material and to minimize degradation due to radiation damage. Data loss will be reduced with a new pixel readout chip (ROC) [3].

The efficiency in the strip tracker is measured using tracks that have a minimum of eight hits in the pixel and strip detectors combined. Once the defective modules are excluded from the measurement, the overall hit efficiency is 99.8%. This number is compatible with the 0.2% fraction of defective channels observed during the construction of the strip tracker.

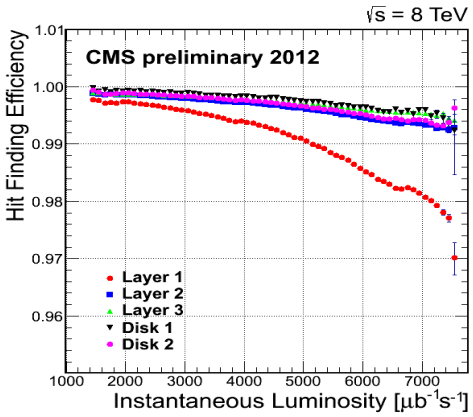

Figure 1: Pixel Hit Finding Efficiency vs Instantaneous Luminosity for all Layers and Disks, as measured with 2012 data.

The hit resolution in the pixel and strip barrel sensors has been studied by measuring residuals, defined by the difference between the measured and the expected hit position as predicted by the fitted track. The measured pixel hit resolution in the $r\phi$ coordinate, is 9.4 μm. The pixel hit resolution in the longitudinal direction depends on the angle of the track relative to the sensor, and ranges from 20 μm to 45 μm.

Sophisticated tracking and vertexing software algorithms reconstruct the data provided by the silicon tracker. The tracking algorithms reconstruct tracks over the full pseudorapidity range of the tracker $|\eta| < 2.5$, finding charged particles with p_T as low as 0.1 GeV, or produced as far as 60 cm from the beam line. Promptly produced, isolated muons of $p_T > 0.9$ GeV are recon-

structed with essentially 100% efficiency for $|\eta| < 2.4$. In the central region ($|\eta| < 1.4$), where the resolution is best, muons of p_T= 100 GeV have resolutions of approximately 2.8% in p_T, and 10 and 30 μm in transverse and longitudinal impact parameter, respectively. For non isolated particles of $1 < p_T < 10$ GeV and $|\eta| < 1.4$, the track resolutions are typically 1.5% in p_T and 25–90 (45–150) μm in the transverse (longitudinal) impact parameter. The primary vertex resolution achieved in typical events of interest is 10–12 μm in all three dimensions [2].

An example of the excellent tracking performance achieved for physics is shown in Fig. 2, showing excellent mass resolution in the dimuon invariant mass spectra around the Upsilon peaks.

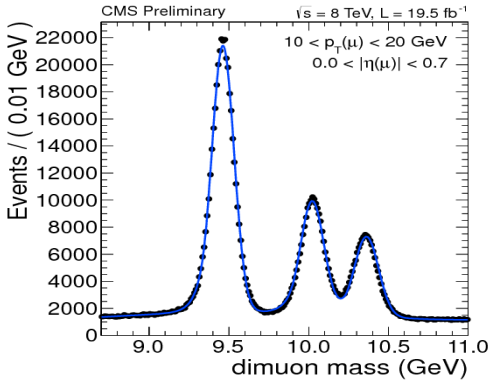

Figure 2: Invariant mass distribution of dimuons in the vicinity of the Υ(nS) resonances, for an integrated luminosity of 19.5 fb^{-1} at $\sqrt{s}$= 8 TeV

During LHC Run 2 the CMS tracker will be operated at low temperature, in order to mitigate possible long term damages. The strip tracker has been tested to temperatures of down to −20 °C, with the plan to operate it a −15 °C. A new sealing with vapour barrier and dry gas flow has been installed to avoid condensation in the tracker volumes and service ducts. The pixel detector has been tested to −25 °C, and will be operated at −20 °C. A test slice of the new forward pixel detector is on track for insertion during LS1.

3. Electromagnetic Calorimeter

The ECAL is a homogeneous crystal calorimeter made of 75848 lead tungstate ($PbWO_4$) crystals. These crystals provide fast response, radiation tolerance and excellent energy resolution. The high-density (8.28 g/cm^3), short radiation length (X_0 = 0.89 cm), and small Molière radius (R_M = 2.2 cm) of $PbWO_4$ allow the construction of a compact calorimeter with fine granularity, and the fast scintillation response allows for excellent time resolution. The detector consists of a barrel region (EB), covering up to pseudorapidity $|\eta|$ =1.48, and two endcaps (EE), that extend the coverage up to $|\eta| = 3.0$. Electron and photon identification is possible up to $|\eta| = 2.5$ - the region covered by the silicon tracker. The lead tungstate crystals are $25.8X_0$ long in the barrel and $24.7X_0$ long in the endcaps. The scintillation light is detected by avalanche photodiodes (APDs) in the barrel region, and by vacuum phototriodes (VPTs) in the endcaps. A preshower detector consisting of two planes of silicon strip sensors interleaved with a total of $3X_0$ of lead is located in front of each EE.

While the crystal scintillation mechanism is not altered by irradiation, the crystal transparency is reduced. The VPT response is affected by the total extracted charge and a signal decrease to a plateau is expected. In order to measure and correct for response changes during LHC operation, the ECAL is equipped with a dedicated light monitoring system. The response change observed in the ECAL channels is up to 6% in the barrel, reaching up to 30% at $|\eta| \approx 2.5$, the limit of the tracker acceptance. The response change is up to 70% in the region closest to the beam pipe [4]. These measurements are used to recalibrate the ECAL signal amplitudes, both offline and at the trigger level.

Different methods are used to intercalibrate the response of ECAL channels [5]. The ϕ-symmetry intercalibration exploits the invariance around the beam axis of the energy flow in minimum bias events. The invariant mass of photon pairs from low mass resonances ($\pi^0 \rightarrow \gamma\gamma$ and $\eta \rightarrow \gamma\gamma$) is also used to calibrate the crystal response. Isolated electrons from $W \rightarrow e\nu$ and $Z \rightarrow ee$ decays are used to compare the energy measured in ECAL to the track momentum measured in the silicon tracker.

In Fig. 3 the precision for measuring the intercalibration constants from the different methods is shown as a function of η in EB, using 2012 data [4]. The precision of the ϕ-symmetry and photon calibrations is at the level of the systematic errors. The precision of the electron calibration is still dominated by the statistical errors for $\eta > 1$. A weighted average of the results of these three methods leads to an optimum inter-crystal calibration, as also shown in Fig. 3. The final intercalibration precision is better than 1% in the EB, and about 2% EE. Absolute calibration is obtained using the $Z \rightarrow ee$ invariant mass peak.

The ECAL energy resolution for electrons with $E_T \approx$45 GeV from Z$\rightarrow e^-e^+$ decays is better than 2%

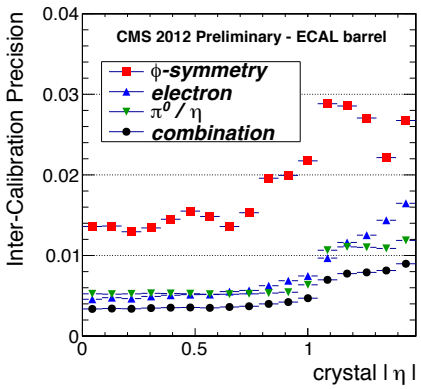

Figure 3: Precision of channel inter-calibration as a function of pseudorapidity in the ECAL barrel

in the central region of the EB ($|\eta| < 0.8$), and is between 2% and 5% elsewhere. For low-bremsstrahlung electrons, where 94% or more of their energy is contained within a 3×3 array of crystals, the energy resolution improves to 1.5% for $|\eta| < 0.8$ [5]. Electron energy resolution is driven by ECAL for E > 15 GeV. Fig. 4 shows the mass resolution of the Z peak, reconstructed from its di-electron decay mode, as a function of time for the EB [4]. The re-reconstruction of data, using a calibration obtained from the full data sample, improves the resolution stability with time in comparison to the already excellent prompt (within 48 hours) reconstruction.

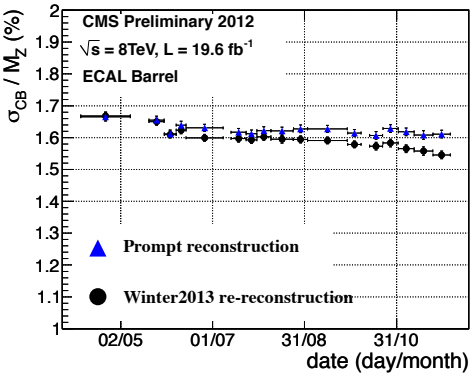

Figure 4: The mass resolution of the Z peak, reconstructed from its di-electron decay mode, as a function of time for the CMS ECAL barrel. The width of the Z peak is fitted with a convolution of a Crystal Ball with a Breit-Wigner line shape. The Gaussian width parameter of the Crystal Ball function is taken as a measure of the mass resolution.

4. Hadronic Calorimeter

The CMS Hadronic calorimeter consist of four sections. The HCAL Barrel (HB) and Endcap (HE) calorimeters cover regions of 0< $|\eta|$ <1.3 and 1.3< $|\eta|$ <3, respectively. Both are sampling calorimeters, made of alternating layers of brass absorber and plastic scintillator tiles, with hybrid photo-detector (HPD) readout. The HCAL Outer (HO) is designed as a tail catcher made of plastic scintillator layers placed outside the CMS solenoid, using the CMS coil as absorber, also with HPD readout. The HCAL Forward (HF) is situated at $|z|$ =11 m covering the range 2.9< $|\eta|$ <5. It is a Cherenkov calorimeter, with light being collected by scintillating quartz fibres inserted in steel absorber, and read out with photomultipler tubes (PMTs). The stability of the detector response, photo-detector gains and signal time synchronization are monitored using LED and laser systems.

In the region $|\eta| < 1.74$, the HCAL cells have widths of 0.087 in pseudorapidity and 0.087 in azimuth. In the η-ϕ plane, and for $|\eta| < 1.48$, the HCAL cells map on to 5×5 ECAL crystals arrays to form calorimeter towers in $\eta - \phi$ space, projecting radially outwards from close to the nominal interaction point. At larger values of $|\eta|$, the η-ϕ size of the towers increases and the matching ECAL arrays contain fewer crystals. Within each tower, the energy deposits in ECAL and HCAL cells are summed to define the calorimeter tower energies, subsequently used to provide the energies and directions of hadronic jets. The HCAL, when combined with the ECAL, measures jets with a resolution $\Delta E/E \approx 100\%/\sqrt{E\,[GeV]} \oplus 5\%$ [5].

The CMS collaboration has developed several distinct and complementary algorithms to reconstruct missing transverse energy ($\vec{E}_{\mathrm{T}}$) [6]. The $\vec{E}_{\mathrm{T}}$ reconstructed using a particle-flow technique (PF $\vec{E}_{\mathrm{T}}$) is used in the majority of CMS analyses due to its high performance [7]. It is calculated as the negative of the vectorial sum over transverse momenta of all particles reconstructed by the particle-flow algorithm.

Jet reconstruction and $\vec{E}_{\mathrm{T}}$ performance has been extensively measured using Run 1 data and simulation [8]. Fig. 5 shows the PF $\vec{E}_{\mathrm{T}}$ distributions for events passing dijet selection, for an integrated luminosity of 11.5 fb^{-1} at $\sqrt{s}$= 8 TeV. The anomalous events observed in data (open black markers) with PF $\vec{E}_{\mathrm{T}}$ around 600 GeV are mainly due to misfires of the HCAL laser calibration system, and the anomalous events with PF $\vec{E}_{\mathrm{T}}$ around 2 TeV are mainly caused by electronics noise in HB and HE. A set of algorithms was developed to exploit

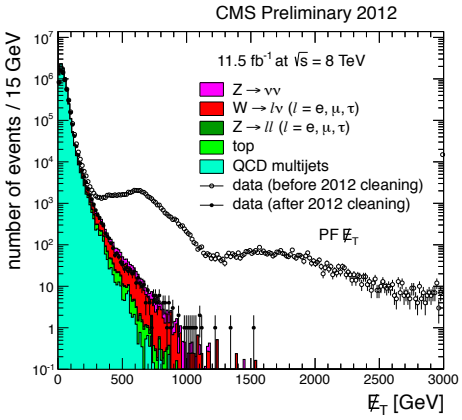

Figure 5: Particle-Flow missing transverse energy distributions for events passing the dijet selection without 2012 cleaning algorithms applied (open markers), with 2012 cleaning algorithms applied including the one based on jet identification requirements (filled markers), and events from MC (filled histograms)

the differences between noise and signal pulse shapes in order to reject noise hits from event reconstruction. The PF $\vec{\not{E}}_{\rm T}$ distribution for events passing (filled black markers) all cleaning algorithms and jet identification requirements shows a substantial reduction of the high PF $\vec{\not{E}}_{\rm T}$ tail.

A set of upgrades of the HCAL began during LS1, in order to improve the performance of jet and energy reconstruction in Run 2. During Run 1 electric discharges were observed in the HCAL HPDs, which were particularly relevant in HO due to the presence of the magnetic fringe field. In addition, analysis of LED data showed time drift of HPD gains. For these reasons all HPDs are planned to be replaced with silicon photomultipliers (SiPM). In particular, the HO detector has already been upgraded with SiPMs during LS1. Validation and calibration is proceeding with cosmic muons, and first results show that muon MIP signals are now clearly visible. In the HF, anomalous signals were produced by particles hitting the PMT windows. These PMT are now being replaced with thinner window, multi-anode readout design, that will mitigate this effect by a significant factor. In addition both HF back-end and front-end electronics will be upgraded in different stages. The front-end electronics will include high precision timing readout, and the back-end electronics will handle the increased data bandwidth. Further HCAL upgrades are planned after Run 2.

5. Muon System

Muon reconstruction in CMS is performed with the all-silicon tracker at the heart of the detector, and with up to four stations of gas-ionization muon detectors installed outside the solenoid and sandwiched between steel layers serving both as hadron absorbers and as a return yoke for the magnetic field. The muon system covers the pseudorapidity region $|\eta| < 2.4$ and performs three main tasks: triggering on muons, identifying muons, and assisting the CMS tracker in measuring the momentum and charge of high $p_{\rm T}$ muons.

Drift Tube (DT) chambers and Cathode Strip Chambers (CSC) are used in $|\eta| < 1.2$ and $0.9 < |\eta| < 2.4$ respectively, complemented by a system of Resistive Plate Chambers (RPC) covering the range of $|\eta| < 1.6$. The basic element of the DT system is the drift cell of 42×13 mm^2. The gas mixture (85%/15% of Ar/CO_2) provides good quenching properties and a saturated drift velocity of about 55 μm/ns. The maximum drift time is almost 400 ns. A CSC consists of 6 layers, and operates as standard multi-wire proportional counters (MWPC). The cathode strips run radially outward and provide a precise measurement in the r$-\phi$ bending plane. The wires provide a coarse measurement in the radial direction. All chambers use a gas mixture of 50% CO_2, 40% Ar, and 10% CF_4. The RPC are double-gap chambers, operated in avalanche mode to ensure reliable operation at high rates, that can provide fast and independent trigger signals. The spatial resolution per chamber was 80–120 μm in the DTs, 40–150 μm in the CSCs, and 0.–1.2 cm in the RPCs. The time resolution achievable was 3 ns or better per chamber for all 3 systems. More details on the CMS muon systems and its performance can be found in [9]

Matching muons to tracks measured in the silicon tracker results in a relative transverse momentum resolution for muons with $20 < p_{\rm T} < 100$ GeV of 1.3–2.0% in the barrel and better than 6% in the endcaps. The $p_{\rm T}$ resolution in the barrel is better than 10% for muons with $p_{\rm T}$ up to 1 TeV [10]

Fig. 6 shows the identification efficiency as function of η for muons with $p_{\rm T}$> 20 GeV passing the CMS Tight Muon Selection, as measured using the tag-and-probe technique with Z$\rightarrow \mu\mu$ decays [11]. The identification efficiency is typically >90% and the simulation models well the data.

Fig. 7 shows hadron to muon misidentification probability versus η for the same tight selection, for pions and protons with p_T >4 GeV [12]. Misidentification probabilities are few per mille for pions, for which the dominant component of the misidentification comes from de-

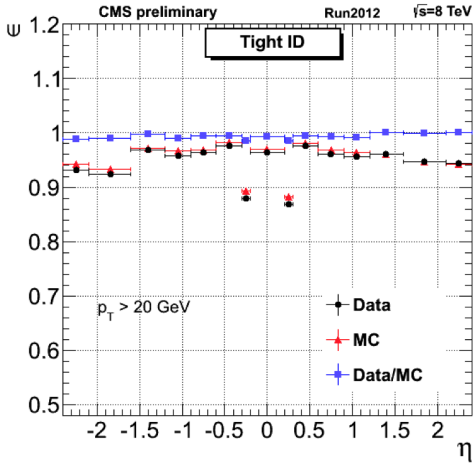

Figure 6: Tag-and-probe results for the muon identification efficiency of the CMS Tight Muon selection as function of η for muons with p_T>20 GeV in $\sqrt{s}$ =8 TeV data compared to simulation

cays in flight, and well below 1 per mille for protons, with misidentification mechanisms being dominated by punch-through and random matching. Results from data and simulation are in good agreement.

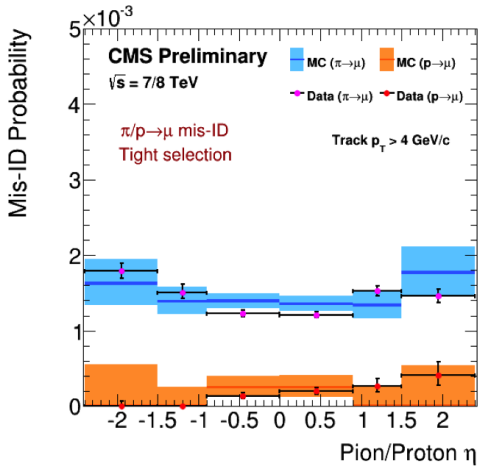

Figure 7: Fraction of pions and protons with p_T >4 GeV misidentified as muons by the Tight Muon selection, in data and simulation.

Thanks to the excellent timing capabilities of the CMS muon system no problems with event pre-firing have been observed at the level of muon triggering during Run 1.

During LS1 general repairs and maintenance work has been performed on the three muon systems. The DT readout and trigger electronics have been moved out of the experimental cavern, in order to gain robustness and allow for flexibility in possible future interventions. New CSC and RPC chambers have been installed in the endcap region, which will result in improvements in muon reconstruction and identification and in reduction of muon trigger rate. Part of the CSC electronics has also been upgraded, allowing in particular exploitation of the full chamber segmentation in 2.1< $|\eta|$ <2.4 and will result in an increase of data-rate capacity for Run 2. Commissioning of the whole muon system is presently ongoing using muons from cosmic rays.

6. The Trigger System

The first level of the CMS trigger system uses information from the calorimeters and muon detectors in custom hardware processors to select the most interesting events in a fixed time interval of less than 4μs [13]. The HLT further decreases the event rate by using the full event information, including that from the silicon tracker [14]. During Run 1, 100 kHz of L1 accepted events was reduced to around 400 Hz by the HLT before data storage.

In order to preserve a sensitivity for electroweak scale physics and for TeV scale searches similar to that achieved before LS1, CMS has planned major optimizations in the L1 and HLT systems, happening during LS1 and throughout Run 2. The L1 trigger system will undergo major modifications, to be implemented in a staged approach, allowing for better lepton isolation and pileup subtraction algorithms. New more powerful electronics will be put in place, offering much improved flexibility compared to the current trigger system. The HLT computer farm will also be upgraded, and new algorithms are being developed, significantly reducing tracking time for the expected conditions in 2015, for example.

7. Beam Radiation Instrumentation and Luminosity Measurement

CMS has specific detectors to measure the luminosity and machine induced background. A new data acquisition system and new detectors will be put in place for Run 2 in order to provide a continuous real-time measurement of the luminosity delivered by LHC to CMS and in order to measure beam losses, with the main purpose of protecting the silicon Pixel and Strip tracking detectors by inducing a beam dump if needed.

8. Global Performance

The characteristics of the CMS detector allow for sophisticated reconstruction algorithms of particle-flow type, of particular relevance for computation of global event quantities, like $\vec{E}_T$. In multi-jet events only ≈10% of the energy goes to neutral stable hadrons. For the rest of the particles in the event entering the $\vec{E}_T$ calculation, the momenta and energies measured by the tracker and ECAL provide better $\vec{E}_T$ resolution than traditional approaches based on calorimetry only. Due to the high magnetic field, charged particles are well separated in the large tracker volume, and the excellent CMS tracking allows the precise measurement of the track momenta down to very low p_T. The high granularity of ECAL permits accurate matching of tracks and calorimeter deposits, and provides excellent energy resolution. Fig. 8 shows the perpendicular recoil component resolution curves for the PF $\vec{E}_T$ and Calo $\vec{E}_T$ algorithms, versus the number of reconstructed vertices for Calo $\vec{E}_T$ for Z→ $\mu\mu$ events [8]. Calo $\vec{E}_T$ is calculated using the energies contained in calorimeter towers and their directions relative to the centre of the detector. Significantly better resolution is achieved with PF $\vec{E}_T$ with respect to Calo $\vec{E}_T$.

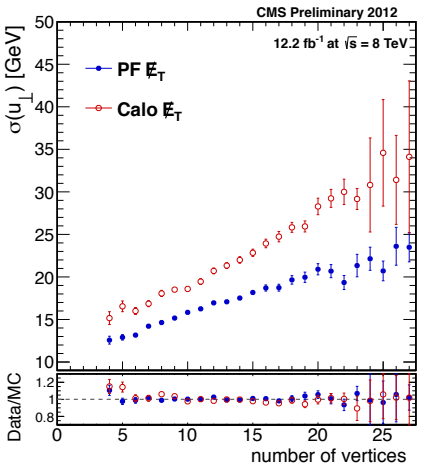

Figure 8: Perpendicular recoil component resolution curves for the PF $\vec{E}_T$ and Calo $\vec{E}_T$ algorithms versus the number of reconstructed vertices for Calo $\vec{E}_T$ for Z→ $\mu\mu$ events.

In CMS particle flow reconstruction is used in the High Level Trigger, resulting in significant rate reductions, in particular for jet and $\vec{E}_T$ triggers. In addition, particle flow reconstruction is the basis for novel algorithms that significantly reduce the sensitivity to pileup.

9. Conclusions

During the LHC Run 1, the CMS detector has shown excellent triggering capabilities and performance in tracking and vertexing, particle identification, reconstruction and energy measurement, as well as in jet and $\vec{E}_T$ reconstruction. This resulted in the highest data quality delivered for final physics analyses. CMS is on track to maintain or, where possible, improve this performance for the LHC Run 2 data taking period.

References

[1] S. Chatrchyan, et al., The CMS experiment at the CERN LHC, JINST 3 (2008) S08004. doi:10.1088/1748-0221/3/08/S08004.
[2] S. Chatrchyan, et al., Description and performance of track and primary-vertex reconstruction with the CMS trackerSubmitted to *J. INST*. arXiv:1405.6569.
[3] CMS Collaboration, CMS Technical Design Report for the Pixel Detector Upgrade, CERN/LHCC 2012-016.
[4] CMS Collaboration, 2012 ECAL detector performance plots, CMS-DP-2013-007 (2013).
[5] S. Chatrchyan, et al., Energy calibration and resolution of the CMS electromagnetic calorimeter in pp collisions at $\sqrt{s}$ = 7 TeV, J. Instrum. 8 (arXiv:1306.2016. CMS-EGM-11-001. CERN-PH-EP-2013-097) (2013) P09009. 51 p, comments: Submitted to JINST.
[6] S. Chatrchyan, et al., Missing transverse energy performance of the CMS detector, JINST 6 (2011) P09001. arXiv:1106.5048, doi:10.1088/1748-0221/6/09/P09001.
[7] CMS Collaboration, Particle–flow event reconstruction in CMS and performance for jets, taus, and $\vec{E}_t$, CMS Physics Analysis Summary CMS-PAS-PFT-09-001.
[8] CMS Collaboration, MET performance in 8 TeV data, CMS Physics Analysis Summary CMS-PAS-JME-12-002.
[9] S. Chatrchyan, et al., The performance of the CMS muon detector in proton-proton collisions at sqrt(s) = 7 TeV at the LHC, JINST 8 (2013) P11002. arXiv:1306.6905, doi:10.1088/1748-0221/8/11/P11002.
[10] S. Chatrchyan, et al., Performance of cms muon reconstruction in pp collision events at $\sqrt{s}$ = 7 TeV, JINST 7 (2012) P10002. arXiv:1206.4071, doi:10.1088/1748-0221/7/10/P10002.
[11] CMS Collaboration, Single Muon efficiencies in 2012 Data, CMS-DP-2013-009 (2013).
[12] CMS Collaboration, Muon Identification performance: hadron mis-Id measurements and RPC Muon selections, CMS-DP-2014-018 (2014).
[13] CMS Collaboration, The TriDAS Project Technical Design Report: The Level-1 Trigger, CERN/LHCC 2000-038.
[14] CMS Collaboration, CMS Data Acquisition and High-Level Trigger Technical Design Report, CERN/LHCC 2002-026.
[15] S. Chatrchyan, et al., Energy calibration and resolution of the CMS electromagnetic calorimeter in pp collisions at $\sqrt{s}$ = 7 TeV, JINST 8 (2013) P09009. arXiv:1306.2016, doi:10.1088/1748-0221/8/09/P09009.
[16] S. Chatrchyan, et al., Performance of CMS muon reconstruction in *pp* collision events at $\sqrt{s}$ = 7 TeV, JINST 7 (2012) P10002. arXiv:1206.4071, doi:10.1088/1748-0221/7/10/P10002.